Automatic Renal Cortex Segmentation Using Implicit Shape Registration and Novel Multiple Surfaces Graph Search

Xiuli Li, Xinjian Chen, Jianhua Yao, Xing Zhang, Fei Yang, and Jian Tian*, *Fellow, IEEE*

***Abstract*—In this paper, we present an automatic renal cortex segmentation approach using the implicit shape registration and novel multiple surfaces graph search. The proposed approach is based on a hierarchy system. First, the whole kidney is roughly initialized using an implicit shape registration method, with the shapes embedded in the space of Euclidean distance functions. Second, the outer and inner surfaces of renal cortex are extracted utilizing multiple surfaces graph searching, which is extended to allow for varying sampling distances and physical constraints to better separate the renal cortex and renal column. Third, a renal cortex refining procedure is applied to detect and reduce incorrect segmentation pixels around the renal pelvis, further improving the segmentation accuracy. The method was evaluated on 17 clinical computed tomography scans using the leave-one-out strategy with five metrics: Dice similarity coefficient (DSC), volumetric overlap error (OE), signed relative volume difference (SVD), average symmetric surface distance (D_{avg}), and average symmetric rms surface distance (D_{rms}). The experimental results of DSC, OE, SVD, D_{avg}, and D_{rms} were $90.50\% \pm 1.19\%$, $4.38\% \pm 3.93\%$, $2.37\% \pm 1.72\%$, $0.14\ \mathrm{mm} \pm 0.09\ \mathrm{mm}$, and $0.80\ \mathrm{mm} \pm 0.64\ \mathrm{mm}$, respectively. The results showed the feasibility, efficiency, and robustness of the proposed method.**

***Index Terms*—Implicit shape registration, multiple surfaces graph searching, physical constraints, renal cortex, segmentation.**

I. Introduction

THE KIDNEY consists of four major internal structures, the renal cortex, renal column, renal medulla, and renal pelvis (see Fig. 1). The renal cortical volume and thickness have been proven to be effective biomarkers for renal function in many clinical situations [1]–[4]. The applications include urological treatment decision-making [1], radiotherapy planning [2], and assessment of clinical outcomes of surgery [3], [4]. Since the information of renal cortical volume and thickness plays an important role in renal function assessment, the renal cortex segmentation is desirable for renal cortical thickness measurement.

Several prior investigations [5]–[17] have addressed the kidney segmentation on different imaging modalities. However, most of them aimed at the whole kidney segmentation and few modeled the specific kidney structures such as the renal column and renal cortex. Xie *et al.* [5] proposed a texture and shape priors based method for whole kidney segmentation on ultrasound (US) images. They were not able to distinguish the different structures within the kidney on the US images. Another disadvantage is that the initial segmentation curves were positioned manually. Lin *et al.* [6] proposed an anatomical model based approach for whole kidney segmentation on computed tomography (CT) images. Limited by the imaging protocol, different kidney structures cannot be easily distinguished on the CT images. Spiegel *et al.* [7] proposed a technique based on nonrigid image registration and active shape model for whole kidney segmentation on CT images. The presented segmentation system was initialized by a seed point at the center of gravity of the image. Freiman *et al.* [8] proposed a nonparametric model constraint graph min-cut algorithm for automatic whole kidney segmentation on CT images. Gloger *et al.* [9] proposed a 3-D segmentation framework for fully automatic kidney parenchyma on magnetic resonance imaging (MRI) images using Bayesian concepts for probability map generation.

In our previous work [10], we proposed a novel graph construction based optimal graph search method for renal cortex segmentation on CT images. The renal cortex segmentation problem was handled as a multiple surfaces extraction problem. The coarse presegmentation was accomplished with the help of Amira [18]. The method was evaluated in terms of true positive volume fraction (TPVF) and false positive volume fraction (FPVF) by comparing the experimental results against manual delineation results. Though the overall performance was positive, the cortex segmentation was often incorrect around the renal pelvis region as stated in [10].

Described below, we will first analyze the challenges in renal cortex segmentation due to the specific anatomical structures of the kidney, as well as the demand of the renal cortex segmentation method. Then, we will review the multiple surfaces graph

Manuscript received April 12, 2012; revised May 31, 2012; accepted May 31, 2012. Date of publication June 08, 2012; date of current version September 27, 2012. This work was supported in part by the National Basic Research Program of China (973 Program) under Grant 2011CB707700, in part by the National Natural Science Foundation of China under Grant 81071218, Grant 60910006, and Grant 30873462, in part by the Knowledge Innovation Project of the Chinese Academy of Sciences under Grant KSCX2-YW-R-262, in part by the Fellowship for Young International Scientists of the Chinese Academy of Sciences under Grant 2010Y2GA03, in part by the Chinese Academy of Sciences Visiting Professorship for Senior International Scientists under Grant 2010T2G36, and in part by the strategic cooperation project jointly funded by Guangdong Province and the Chinese Academy of Sciences 2010A090100032. *Asterisk indicates corresponding author.*

X. Li, X. Zhang, and F. Yang are with the Intelligent Medical Research Center, Institute of Automation, Chinese Academy of Sciences, Beijing 100190, China.

X. Chen and J. Yao are with the Radiology and Imaging Sciences Department, Clinical Center, National Institute of Health, Bethesda, MD 20814 USA.

*J. Tian is with the Intelligent Medical Research Center, Institute of Automation, Chinese Academy of Sciences, Beijing 100190, China (e-mail: tian@ieee.org).

Color versions of one or more of the figures in this paper are available online at http://ieeexplore.ieee.org.

Digital Object Identifier 10.1109/TMI.2012.2203922

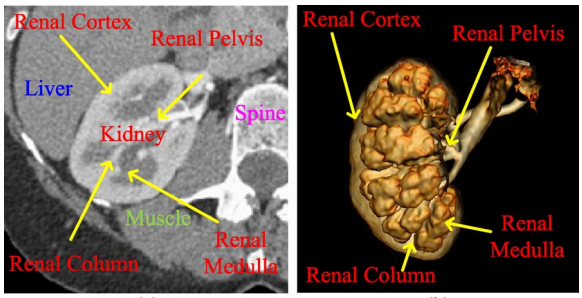

Fig. 1. Anatomical structures of kidney. (a) CT image of the kidney. (b) Kidney iso-surface rendering.

search and draw forth our extensions to the method which improves the renal cortex segmentation. The last will be the overall contributions of our work.

A. Challenges in Renal Cortex Segmentation

CT imaging is widely used for kidney examination and diagnosis since essential anatomical information, including kidney morphology and kidney ducts, can be readily appreciated. We can perceive the location of kidney in abdomen and its specific internal anatomical structures from CT image [see Fig. 1(a)] and the surface rendering of different kidney tissues [see Fig. 1(b)]. The right kidney in Fig. 1 is located on the right side of the spine, below the diaphragm and posterior to the liver.

In Fig. 1, we can find several special characteristics of the kidney's anatomical structure.

1) The boundaries with adjacent organs (e.g., liver, spine, and muscles) are weak. Image artifacts, noise, and various pathologies, such as tumors and nephrolithiasis often exist.
2) The renal cortex and renal column are almost fused as one connected component, which is due to the fact that they have very similar intensity distributions.
3) The renal pelvis makes the renal cortex a nonfully closed structure.

These special characteristics make renal cortex segmentation a challenging task. Traditional methods such as region growing and thresholding will be likely to fail. In order to overcome the weak boundaries, graph-based methods can be employed to search for a global optimal solution. Countering the intensity proximity of the renal cortex and renal column, the model-based methods incorporating anatomical constraints are needed to separate the renal cortex and renal column. Since the renal cortex is nonfully closed around the renal pelvis, a renal cortex refining procedure is required to remove the nontarget region and improve the renal cortex segmentation.

A novel optimal surface search method [10] had already been applied to segment the renal cortex by simultaneously extracting its outer and inner surfaces. The optimal surface search method starts with a coarse presegmentation of the image which yields a robust approximate surface of the object. According to the preceding analysis of the kidney's anatomical structure, the shape model based method other than the intensity based method should be used in the coarse level kidney segmentation. A major component of the shape model based segmentation is the initial estimation of the model pose. Although there already exist several model initialization approaches as reviewed in [19], such as the generalized Hough transform (GHT) [20], [21], evolutionary algorithms (EA) [22], [23] and particle filtering [24], few of them can be applied to the segmentation of the kidney due to the special characteristics of the kidney's anatomical structure. In this work, we propose an implicit shape registration method for kidney shape initialization.

B. Multiple Surfaces Graph Search

Li *et al.* [25] developed a 3-D/4-D graph-based optimal surface detection method which is capable of detecting multiple interacting surfaces simultaneously. As presented in [25]–[27], the multiple surfaces graph search method starts with a coarse presegmentation of the imaging data which yields robust approximate surfaces of the object. Then, a problem-specific graph is constructed holding all relationships and surface cost elements, with intra-surface and inter-surface relationships represented by context-specific graph arcs. Lastly, the traditional graph cut algorithm [28] can be applied to recover optimal surfaces with a low-order polynomial time complexity. Overall, the surface segmentation problem can be modeled by a complex multi-layer s-t graph in which solution related costs are associated with individual graph nodes.

After analyzing the challenges in renal cortex segmentation, we found that the original formulation of the multiple surfaces graph search cannot be directly applied to the renal cortex segmentation problem. However, one extension has already been shown to be useful in our preliminary work [10]. In this study, in order to better restrain the intensity proximity of the renal cortex and renal column, we extend the multiple surfaces graph search approach to allow for varying sampling distances and physical separation constraints, instead of the traditional fixed sampling distance and numerical separation constraints. After these improvements, the multiple surfaces graph search could better accommodate the renal cortex segmentation problem.

C. Contributions of Our Work

Overall, we present a fully automatic renal cortex segmentation framework in this paper. Compared to our previous method [10], our novelties are as follows. 1) We employ an implicit shape registration [29] based initialization method which makes the renal cortex segmentation fully automatic. 2) In order to better separate the renal cortex and renal column (detailed in Section I-A), we extend the multiple surfaces graph search to allow for varying sampling distances and physical separation constraints [30], instead of the traditional fixed sampling distance and numerical separation constraints [10], [25]–[27]. 3) A renal cortex refining procedure is further applied to detect and diminish incorrect segmentation pixels around the renal pelvis.

II. Method: Overview

The proposed method is a coarse to fine segmentation approach which consists of four major steps: 1) preprocessing, 2) initialization using implicit shape registration, 3) multiple surfaces graph searching, and 4) renal cortex refining. Fig. 2 shows the framework of the proposed method. First, enhanced volume and average kidney shape are obtained through nonlinear diffusion filtering and shape model training respectively. Then, an implicit shape registration method is applied to initialize the

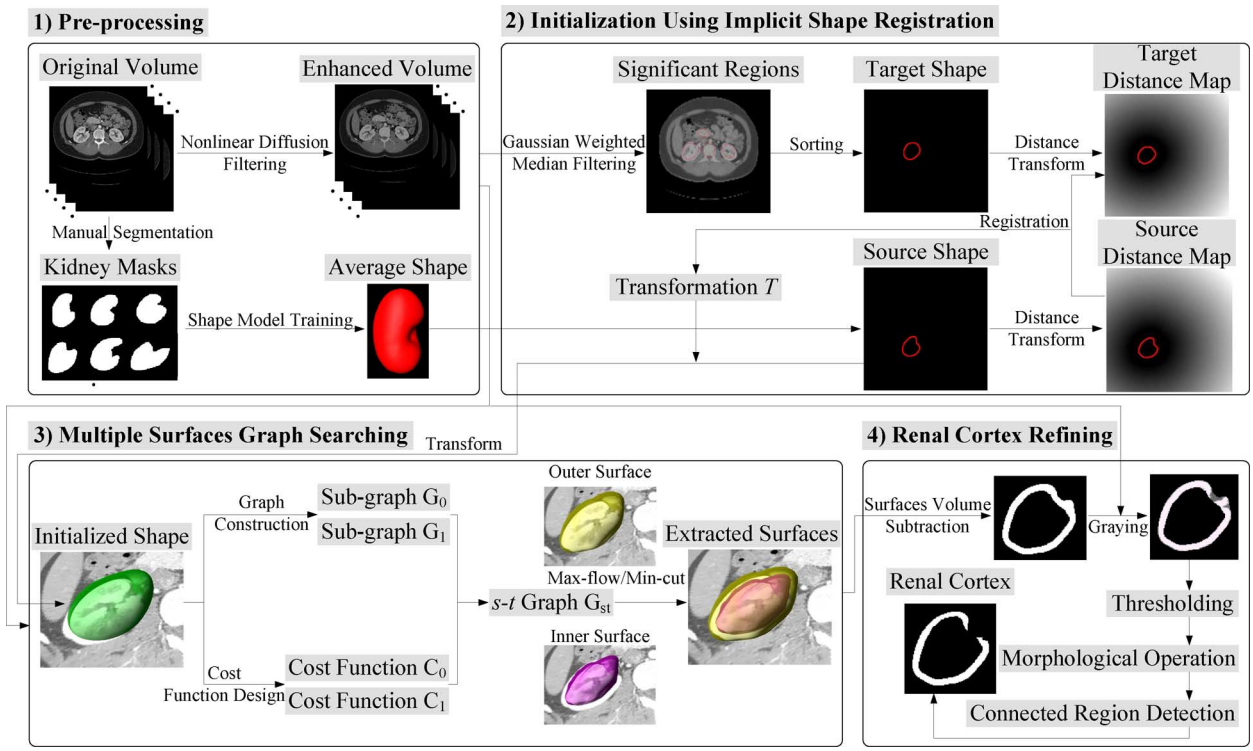

Fig. 2. Framework of the method.

kidney shape in the test scans. These two steps will be described in Section III. Section IV will illustrate in detail how to use the extended multiple surfaces graph search method to recover the outer and inner surfaces of renal cortex. The last is to extract the renal cortex volume based on the outer and inner surfaces, and it will be presented in Section V.

III. Initialization Using Implicit Shape Registration

Acting as an important role in our method, the initialization provides a presegmented surface for the multiple surfaces graph searching and makes our approach fully automatic. Before the initialization, an image preprocessing procedure is applied to enhance the CT volume and construct the average kidney shape model.

A. Preprocessing

Preprocessing includes two parts: nonlinear diffusion filtering and kidney shape model training.

1) Nonlinear Diffusion Filtering: Renal cortex segmentation is initiated by applying a nonlinear diffusion filter [31] to smooth the image and reduce noise. The diffusion filter is defined by following equations:

$$\begin{cases} \frac{\partial u(x,y,z,t)}{\partial(t)} = div[g(|\nabla u|^2)\nabla u] \\ u(x,y,z,0) = u_0(x,y,z). \end{cases} \quad (1)$$

(x, y, z) is the image pixel location and $u(x, y, z, t)$ is a filtered image, where t is a scale parameter. The diffusivity function $g(s) = 1 - \exp(-3.6150/(s/\lambda)^{10})$ if $s > 0$, and $g(s) = 1$ otherwise, λ is the contrast parameter. A sample result of the filter is shown in Fig. 3. We can better perceive the intensity proximity of the renal cortex and renal column from Fig. 3(b) in contrast to Fig. 3(a). The final binary renal cortex segmentation result (detailed in Section V) is presented in Fig. 3(c) for a better contrast effect.

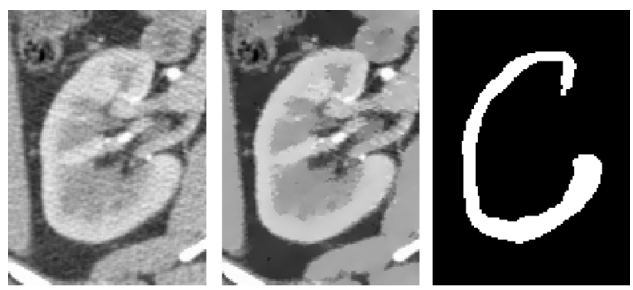

Fig. 3. Example of the renal cortex segmentation. (a) Original image. (b) Enhanced image using nonlinear diffusion filtering. (c) Final binary renal cortex segmentation.

2) Shape Model Training: The kidney shape model is built from manually segmented kidneys in a training set (see Fig. 4). First, triangulated meshes are reconstructed from the manually labeled images using marching cubes [32]. Then, a minimum description length (MDL) [33] approach is used to determine point-wise correspondences for all training shapes. Subsequently, all training shapes are aligned with affine transformations. Finally, the average kidney shape (the "Average Shape" in Fig. 2) can be obtained by $\overline{\Phi} = \sum_i \Phi_i/n$, where Φ_i is a training surface, and n is the number of the training set.

B. Initialization Using Implicit Shape Registration

Although there already exist several model initialization approaches as reviewed in [19], few of them can be applied to

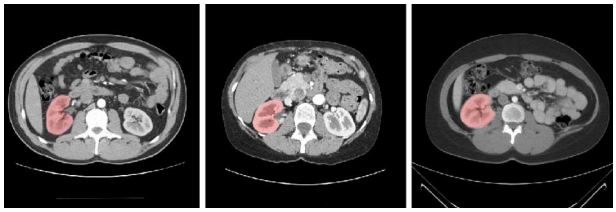

Fig. 4. Training set: right kidney masks in three CT images (red regions).

the segmentation of kidney due to the special characteristics of the kidney's anatomical structure as discussed in Section I-A. In this work, we propose an implicit shape registration method for kidney shape initialization. Before the registration, the contour of the kidney is first detected, to which the average shape will be registered and the model is initiated.

1) Kidney Contour Detection: It is aimed at roughly identifying the contour of the kidney. Since the kidney is a macroscopic region with a relatively high value in contrast-enhanced CT images (see Fig. 1), we apply blurring and thresholding to generate a binary mask of the dataset, which contains several disjointed significant regions. For the blurring, we use the Gaussian weighted median filter [34] for its edge preservation properties that ensure that the significant regions are well separated after thresholding. On the other hand, the extent of fuzziness can be easily tuned through the standard deviation of the Gaussian kernel.

Given a threshold t, the mask volume is generated as follows:

$$M_t(x,y,z) = H(G(x,y,z) * H(I(x,y,z) - t) - 0.5) \quad (2)$$

where $G(x,y,z)$ is the 3-D isotropic Gaussian kernel, i.e., $G(x,y,z) = (1/(2\pi)^{3/2}\sigma^3)e^{-(x^2+y^2+z^2)/2\sigma^2}$, and σ is the standard deviation. $I(x,y,z)$ represents the intensity of pixel (x,y,z), and $H(u)$ is a standard unit step function: $H(u) = 1$ if $u > 0$, and $H(u) = 0$ otherwise.

According to (2), the process can be implemented in three steps. First, we apply a threshold t to original image to generate an initial binary mask. Second, the linear Gaussian filtering is applied to the mask image. Finally, we use a fixed threshold at 0.5 to extract the final binary mask with significant regions. The main advantage of this approach is the efficiency. On an appropriate down-sampled dataset, it can provide immediate feedback not only in response to the change in threshold t, but also to the change in standard deviation σ. The initial value of t is set empirically at a value where 5% of all voxels are sorted out, and the standard deviation σ is set at 10 mm initially.

After the above process, the resulted binary mask typically contains only a few disjointed significant regions including the kidney regions and the spine region (red contours on the "Significant Regions" in Fig. 2). Then, the right kidney can be sorted out (the "Target Shape" in Fig. 2) by taking the three biggest regions and selecting the rightmost one. This strategy works well on all of our datasets.

2) Implicit Shape Registration: With the preceding process, the kidney contour has been roughly identified on the binary mask images. Since the identified kidney contour only estimates the kidney location with incomplete shape information, this can be perceived by comparing the target shape and source shape

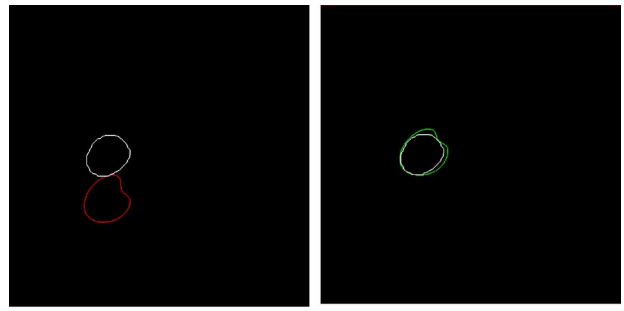

Fig. 5. (a) Initial condition (target shape in white, source shape in red). (b) Registration result, the transformed source shape (in green) is shown overlaid on the target shape (in white).

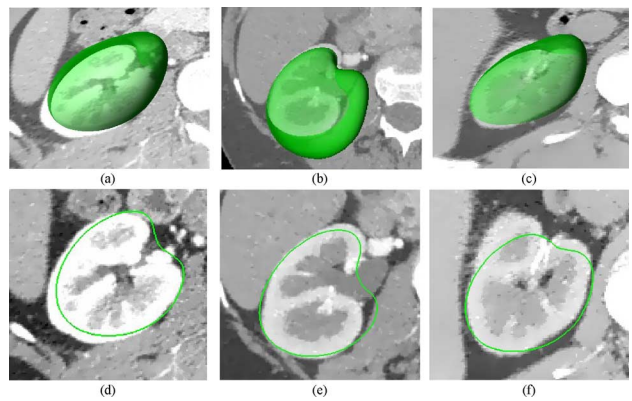

Fig. 6. Initialized shapes. The top row is 3-D surface view, and the bottom row is the 2-D slice view. Both the green semitransparent surfaces and the green lines represent the initialized shapes.

in Fig. 5 (the target shape turns out to be suborbicular); a registration between the source shape (average kidney which stands for the kidney shape information) and the target shape (detected kidney which stands for the kidney location information) is expected to restore both the location and the shape information.

The shapes are represented in an implicit form [35], embedded in the space of Euclidean distance functions (the "Target Distance Map" and "Source Distance Map" in Fig. 2). Such a representation has been widely used in the shape registration task [29], [36] since it is robust, efficient and invariant to rotation and translation. Let $\Phi : \Omega \rightarrow R^+$ be a Lipschitz function that refers to the distance transform of shape S. The shape defines a partition of the image domain Ω: the region S whose points are exactly shape (red contours on the "Target Distance Map" and "Source Distance Map" in Fig. 2), the region R_S that is inside of the shape and the background region $[\Omega - R_S]$. The following implicit shape representation is considered:

$$\Omega_S(p) = \begin{cases} 0, & p \in S \\ -D(p,S) < 0, & p \in R_S \\ +D(p,S) > 0, & p \in [\Omega - R_S] \end{cases} \quad (3)$$

where $D(p,S)$ refers to the minimum Euclidean distance between the point p and shape S.

Then the registration is equivalent to recovering the parameters $\Theta = (\theta_1, \theta_2, \ldots, \theta_N)$ of a parametric transformation T, such that the mean square between the target distance map and

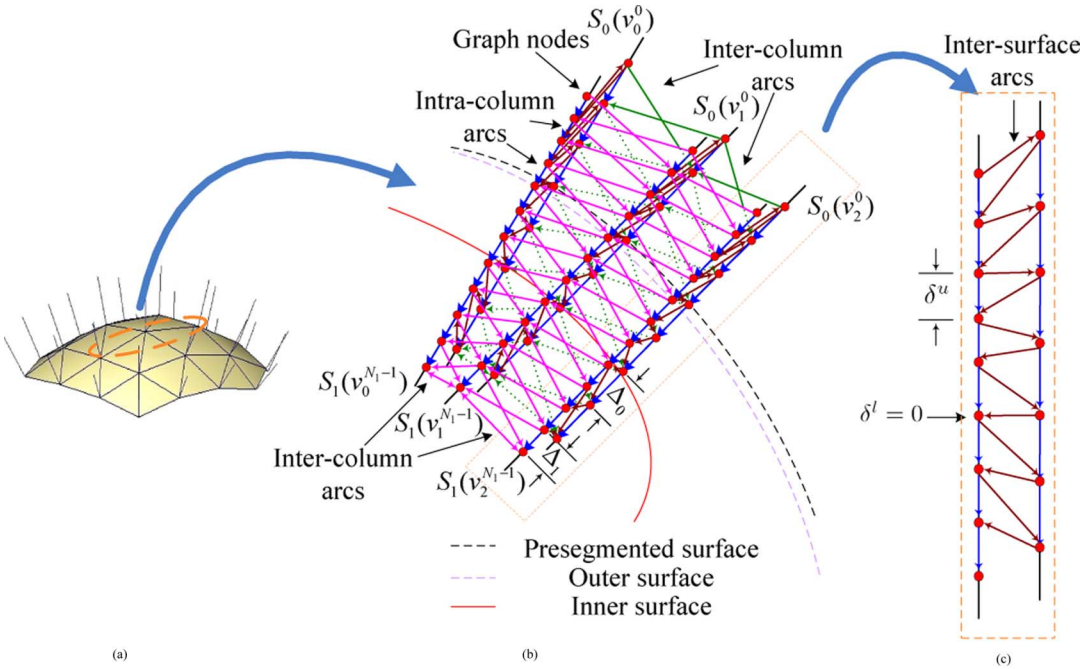

Fig. 7. Graph construction. (a) Triangulated surface mesh with a normal vertex. (b) Graph construction with three columns in the orange ellipse in (a). The whole graph is composed of two sub-graphs G_0 and G_1. The blue edges denote the intra-column arcs, while the green edges and red edges denote the inter-column arcs of the two sub-graphs, and the brown edges between the two columns projected from the same vertex denote the inter-surface arcs. (c) Details of the inter-surface arcs.

source distance map is minimized. This procedure is accomplished with a standard volume-to-volume rigid registration based on a medical image processing and analysis system [37] (3DMed http://www.mitk.net/). We use gradient descent as the optimization method, mean square as the similarity metric and bilinear image interpolation. After registration, the recovered transformation T is applied to the source kidney shape model again, and it leads to the final kidney shape initialization as shown in Fig. 6.

IV. Multiple Surfaces Graph Searching

Multiple surfaces graph searching is the key part in our method whose purpose is to precisely extract the outer and inner surfaces of the renal cortex based on the initialized kidney shape model. The multiple surfaces graph searching can be considered as an optimization process aimed at finding the set of surfaces with a minimal cost. It effectively integrates the shape information with the globally optimal 3-D delineation capability of the graph cut method [28]. The three major components are graph construction, cost function design and optimal surfaces recovery. Graph construction and cost function design are usually carried out in one step to effectively reflect the properties and inter-relationship of the surfaces. After the graph is constructed, the optimal surfaces can be recovered by applying the traditional graph cut algorithm [28].

A. Graph Construction

After prerequisite segmentation of the whole right kidney surface s', a weighted directed graph G is constructed in a narrowband around s'. Unlike the traditional graph construction algorithms which built one single graph for the entire image [25]–[27], our graph construction scheme enables the construction of different sub-graphs according to different surface properties and inter-surface relationships [10]. In this case, graph G consists of two sub-graphs (G_0, G_1) which represent the outer and inner surfaces of the renal cortex respectively. The graph construction process is illustrated in Fig. 7. For each vertex v_j on the mesh, a column of equidistant points is sampled along the normal direction of vertex $\overrightarrow{n_j}$. The sample points are denoted as $S_i(v_j^k), i = 0, 1; j = 1, \ldots, M-1; k = 0, \ldots, N_i$ constituting the nodes for graph G, where i is the index of the two sub-graphs (G_0, G_1), j is the index of the vertex on the surface, and k is the index of the sampled points along the columns.

The interval of the equidistant points is the sampling distance d. In the previous method [10], [25]–[27], all columns have the same single fixed sampling distance as shown in Fig. 8(b). According to the *a priori* information of renal cortex thickness from the training set values and clinicians' experience, and the surface reconstruction technique [33] we use for the shape model construction, the distance between the outer surface and inner surface of one renal cortex tends to be proportional to the sparsity of the local triangular mesh. As a result, incorrect local surface propagation, such as under segmentation as shown in Fig. 9(a) and (c) and over segmentation as shown in Fig. 9(b) and (d) may occur with a fixed sampling distance setting. To address this issue, we compute the sampling distance d_j for each column with $d_j = \sum_a L_{(j,j_a)}/n_j$, where points v_j and v_{j_a} are adjacent on surface s', $L_{(j,j_a)}$ is the vector length from v_j to v_{j_a}, and n_j is the number of points which are adjacent to v_j. The function is proportional to the sparsity of the local triangular mesh and means that the denser the local triangular

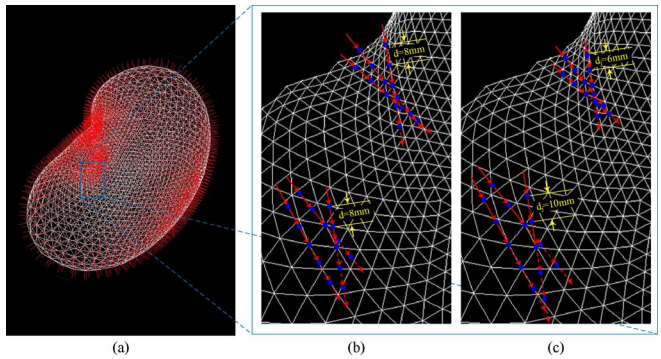

Fig. 8. Sampling distance. (a) The presegmented triangular mesh s' with normal columns. (b) Fixed sampling distance, $d = 8$ mm for all the columns. (c) Varying sampling distances, $d_j = 10$ mm for the columns on a sparser triangular mesh (lower left triangle) and $d_j = 6$ mm for the columns on a denser triangular mesh (upper right triangle).

mesh, a smaller d_j is used, as illustrated in Fig. 8(c). Particularly, the segmentation error around the renal pelvis as shown in Fig. 9(a) and (c) will be greatly reduced with a renal cortex refining procedure in the following Section V.

After the sampled points are obtained, the columns in sub-graphs G_0 and G_1 should be formed based on their properties

$$\begin{cases} S_0(v_j^k) = v_j - \left(k - \frac{(N_0-1)}{2}\right) \cdot d_j \cdot \Delta_0 \cdot \overrightarrow{n_j} \\ \qquad\qquad (k = 0, \ldots, N_0 - 1) \\ S_1(v_j^k) = v_j - \left(k - \frac{(N_1-1)}{2}\right) \cdot d_j \cdot \Delta_1 \cdot \overrightarrow{n_j} \\ \qquad\qquad (k = 0, \ldots, N_1 - 1). \end{cases} \tag{4}$$

The normal direction $\overrightarrow{n_j}$ points outward, and (Δ_0, Δ_1) are the smoothness constraints for the two sub-graphs (G_0, G_1); the symbols $D_{\Delta_0} = d_j \cdot \Delta_0$ and $D_{\Delta_1} = d_j \cdot \Delta_1$ represent the corresponding actual spatial smoothness constraints. These different smoothness constraints determine different sub-graph construction. The surfaces are searched both inward and outward, which is different from our previous work [10]. In contrast to the manual initialization of the kidney shape model in our previous work [10], this search mechanism ensures the segmentation system works well even if some part of the automatically initialized kidney surface is located inside of the renal cortex. The scheme is illustrated in Fig. 7(b) and (c).

In Fig. 7, there are three types of arcs in graph G as denoted in (5), shown at the bottom of the page, where (i, j, k) are the indices defined above, and the three types of arcs are: the intra-column arc E^a connecting two adjacent points on the same column (blue edges in Fig. 7); the inter-column arcs E_i^r connecting two points on two adjacent columns of sub-graph G_i (green edges for E_0^r and red edges for E_1^r in Fig. 7); and

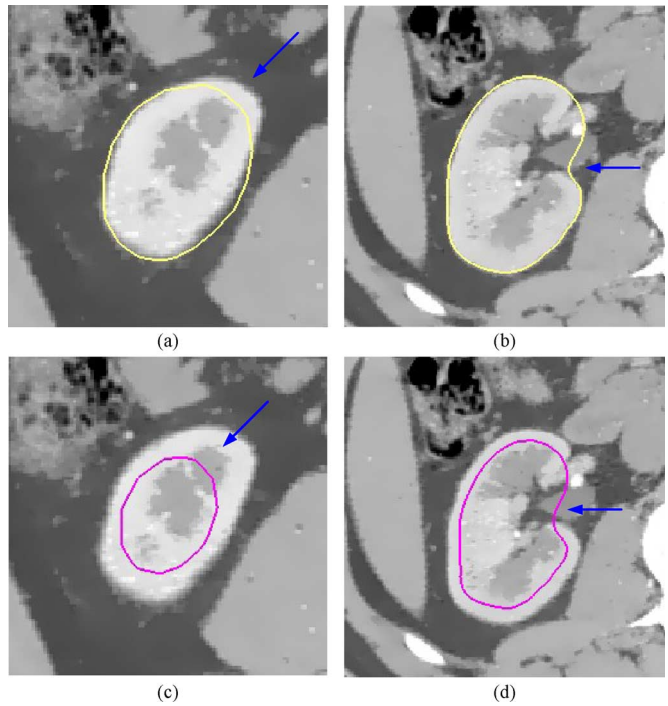

Fig. 9. Examples of under segmentation and over segmentation, the yellow lines denote the outer surface contours of renal cortex, and the purple ones denote the inner surfaces accordingly, while the blue arrows indicate incorrect local surface propagation. (a) Under segmentation of the outer surface. (b) Over segmentation of the outer surface. (c) Under segmentation of the inner surface. (d) Over segmentation of the inner surface.

the inter-surface arcs E^s connecting two points on different sub-graphs (brown edges in Fig. 7). Two smoothness constraints (Δ_0, Δ_1) are designed for the inter-column arcs in each sub-graph reflecting the allowed changes along the normal direction $\overrightarrow{n_j}$, and separation constraints (δ^l, δ^u) exerted on the inter-surface arcs represent the minimal (l means lower) and maximal (u means upper) distances to separate the two surfaces; however, the symbols $D_{\delta_l} = d_j \cdot \delta_l$ and $D_{\delta_u} = d_j \cdot \delta_u$ represent the corresponding actual spatial separation constraints, where d_j is the varying sampling distance defined above.

In previous method [10], [25]–[27], the fixed sampling distance d was used as a unit of measure for the constraints. That means the actual spatial smoothness constraints and spatial separation constraints are

$$\begin{cases} (D_{\Delta_0}, D_{\Delta_1}) = d \cdot (\Delta_0, \Delta_1) \\ (D_{\delta_l}, D_{\delta_u}) = d \cdot (\delta_l, \delta_u). \end{cases} \tag{6}$$

Considering the challenges in renal cortex segmentation as discussed in Section I-A, we bring a concept of physical constraints into the inter-surface relationships, instead of the tradi-

$$\begin{cases} E^a = \{\langle S_i(v_j^k), S_i(v_j^{k-1})\rangle | i = 0, 1; j = 0, \ldots, M-1; k = 1, \ldots, N_i\} \\ E_i^r = \{\langle S_i(v_p^k), S_i(v_q^{\max(0, k-\Delta_i)})\rangle | \forall v_p, v_q \text{ is adjacent; } i = 0, 1; k = 1, \ldots, N_i\} \\ E^s = \{\langle S_1(v_j^k), S_0(v_j^{k_l})\rangle, \langle S_0(v_j^{k_u}), S_1(v_j^k)\rangle | d_j \cdot \delta^l < (S_1(v_j^k) - S_0(v_j^{k_u}), S_1(v_j^k) - S_0(v_j^{k_l})) < d_j \cdot \delta^u\} \end{cases} \tag{5}$$

tional numerical separation constraints to better restrain the intensity proximity of the renal cortex and renal column and eventually separate the renal cortex and renal column. The physical constraint will be learned from *a priori* renal cortex thickness: we first define a variation of renal cortex thickness $[T_{\min}, T_{\max}]$ according to the training set values and clinicians' experience (the defined thickness range is always much bigger than the true value), while satisfying $[D_{\delta_l}, D_{\delta_u}] \subseteq [T_{\min}, T_{\max}]$; then, we compute the corresponding separation constraints with the formulas below

$$\begin{cases} d_j \cdot \delta_l \geq T_{\min}, \\ d_j \cdot \delta_u \leq T_{\max}. \end{cases} \Longrightarrow \begin{cases} \delta_l = \left\lceil \frac{T_{\min}}{d_j} \right\rceil \\ \delta_u = \left\lfloor \frac{T_{\max}}{d_j} \right\rfloor \end{cases} \tag{7}$$

where the symbol $\lceil * \rceil$ denotes the ceiling function and $\lfloor * \rfloor$ denotes the floor function. Then the actual spatial separation constraints are

$$(D_{\delta_l}, D_{\delta_u}) = d_j \cdot (\delta_l, \delta_u) = d_j \cdot \left(\left\lceil \frac{T_{\min}}{d_j} \right\rceil, \left\lfloor \frac{T_{\max}}{d_j} \right\rfloor \right). \tag{8}$$

Comparing (6) and (8), the required parameters (δ_l, δ_u) in previous method [10], [25]–[27] are determined by experience, while the current parameters $[T_{\min}, T_{\max}]$ are learned from *a priori* information of renal cortex thickness.

B. Cost Function Design

The multiple surfaces graph searching is driven by the cost functions associated with the graph vertices, which reflect some properties of the relevant surfaces. All of the intra-column, inter-column and inter-surface arcs are viewed as *n-links* in the s-t graph [28] and assigned infinity values initially. Each node has a weight $W_i(v_j^k)$ in the weighted directed graph G, where (i, j, k) are the indices defined above. If $W_i(v_j^k) \geq 0$, nodes are connected to the sink terminal t by a directed edge with weight $W_i(v_j^k)$, otherwise nodes will be connected to the source terminal s by a directed edge with weight $-W_i(v_j^k)$. These arcs are viewed as *t-links*. The sink terminal t and source terminal s correspond to the background and object labels that can be assigned to pixels, respectively.

Concretely, the node weight $W_i(v_j^k)$ is defined below

$$W_i(v_j^k) = \begin{cases} C_i(v_j^k), & k = 0 \\ C_i(v_j^k) - C_i(v_j^{(k-1)}), & \text{otherwise}, \end{cases} \tag{9}$$

where the cost $C_i(v_j^k)$ is defined with corresponding cost functions. $C_0(v_j^k)$ and $C_1(v_j^k)$ represent the two cost functions for sub-graphs G_0 and G_1 respectively. Generally, the outer surface of the renal cortex can be identified by the image intensity differences between the kidney and surrounding regions. Consequently, a relatively simple cost function—the negated gradient magnitude [38] is used for detecting the outer surface of the renal cortex

$$C_0(v_j^k) = -|\nabla I(v_j^k)|. \tag{10}$$

As stated in Section I-A, since the renal cortex and renal column have very similar intensity distributions, the traditional graph cut algorithm would segment these two different structures as one connected component (Figs. 1 and 10). We test a few filters to separate the two structures. Fig. 10 demonstrates the experimental results of several filters applied to the kidney images. Comparing the three rows in Fig. 10, we find that the experimental results vary according to the image quality, such as image noise and inhomogeneity. Comparing the four columns in Fig. 10, we find that the gradient magnitude filter causes depression of the boundaries between the renal cortex and renal column [see the red arrows in Fig. 10(d)–(f)]; the Sobel edge filter also misses parts of the renal cortex inner contours [see the red arrows in Fig. 10(g)–(i)]. To accommodate the specific attributes of the renal cortex, an enhancement filter which can enhance the annular renal cortex region and depress the projection shaped renal column should be adopted.

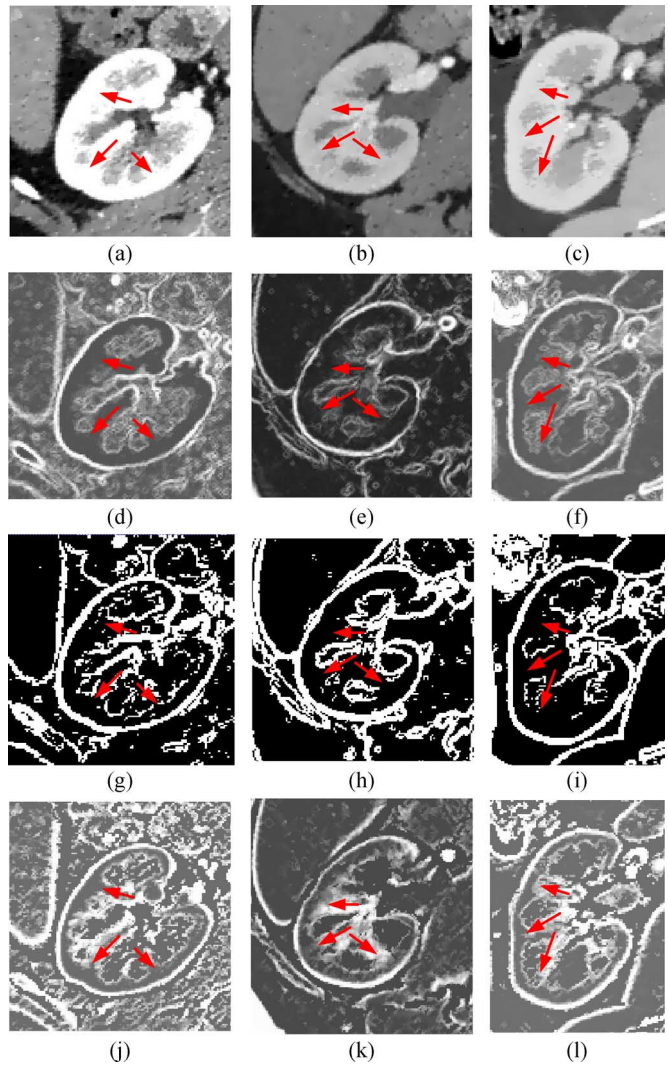

Fig. 10. Experimental results for different filters. Each column represents the experimental results for one kidney data corresponding to the three images in Fig. 6. From left to right, it presents a relatively low quality case (left), a relatively high quality case (middle), and an average case (right). The red arrows indicate the junctions of the renal cortex and renal column. (a)–(c) The enhanced images from Section III-A. (d)–(f) The gradient magnitude images of (a)–(c). (g)–(i) The Sobel edge images of (a)–(c). (j)–(l) The 3-D "sheet filter" of (a)–(c).

Inspired by the work of Sato *et al.* [39], we adopted the 3-D "sheet filter" F_{sheet} for detecting the inner surface of renal

cortex. The 3-D "sheet filter" is based on the Hessian matrix eigenvalues of the volume intensity function combined with isotropic Gaussian blurring to enhance the 3-D local intensity structures. The filter is defined by the following equation:

$$F_{\text{sheet}}(I) = \begin{cases} |\lambda_3| \cdot w(\lambda_2;\lambda_3) \cdot w(\lambda_1;\lambda_3), & \lambda_3 < 0 \\ 0, & \text{otherwise} \end{cases} \quad (11)$$

where $(\lambda_1, \lambda_2, \lambda_3)$ are three eigenvalues of the Hessian matrix $\nabla^2 I$ satisfying $\lambda_1 \geq \lambda_2 \geq \lambda_3$. The derivative computation for the Hessian matrix is combined with Gaussian convolution [40], and the standard deviation σ_f controls the width of the structures. The parameter w is written as

$$w(\lambda_s;\lambda_t) = \begin{cases} \left(1 + \frac{\lambda_s}{|\lambda_t|}\right)^{\gamma}, & \lambda_t \leq \lambda_s \leq 0 \\ \left(1 - \alpha \cdot \frac{\lambda_s}{|\lambda_t|}\right)^{\gamma}, & \frac{|\lambda_t|}{\alpha} > \lambda_s > 0 \\ 0, & \text{otherwise} \end{cases} \quad (12)$$

where γ and α are the parameters that control the sensitivity of the filter to the eigenvalue measures. The theoretical basis for the filter is based on the intensity curvatures predicted for the "sheet" structure: fissures have one large negative eigenvalue $\lambda_3 \ll 0$ corresponding to the eigenvector normal to the fissure plane, and two small eigenvalues $\lambda_1 \approx \lambda_2 \approx 0$ corresponding to the eigenvectors parallel to the plane.

Thus, we use the 3-D "sheet filter" F_{sheet} as the cost function for the inner surface of renal cortex

$$C_1(v_j^k) = -F_{\text{sheet}}(I(v_j^k)). \quad (13)$$

From Fig. 10(j)–(l), we find the annular renal cortex region, especially the boundaries between the renal cortex and renal column, is enhanced after the employment of the 3-D "sheet filter" F_{sheet}.

C. Optimal Surfaces Recovery

After the above two parts, a s-t graph G_{st} is derived from the weighted directed graph G. Segmentation of outer and inner surfaces of the renal cortex is formulated as finding a minimum closed set in the s-t graph G_{st} [25]. This can be solved by computing the minimum s-t cut of the graph using a traditional graph cut algorithm [28], which can simultaneously get both the optimal outer surface and inner surface of the renal cortex while satisfying all surface constraints. Results of the extracted outer and inner surface contours are shown in Fig. 11, optimized from the initialized shapes in Fig. 6.

V. Renal Cortex Refining

Renal pelvis makes the renal cortex a nonfully closed structure and introduces incorrect segmentation pixels around the renal pelvis as stated in our previous work [10]. A renal cortex refining procedure is needed to address this issue and improve the renal cortex segmentation. In this work, the refining procedure consists of the following operations.

A. Surface Volumes Subtraction and Graying

We first voxelize the outer and inner surfaces of the renal cortex into volumes with the same dimensions and spacing as the original CT datasets. Then, a binary renal cortex mask is obtained by subtracting the inner surface volume from the outer surface volume. As we can see from Fig. 1(a), the intensities of renal cortex are much different with those of renal pelvis and the region nearby. By graying the binary renal cortex mask, we can discover the nontarget region intuitively. A simple graying strategy just multiplies the enhanced volume (the "Enhanced Volume" in Fig. 2) by the binary renal cortex mask.

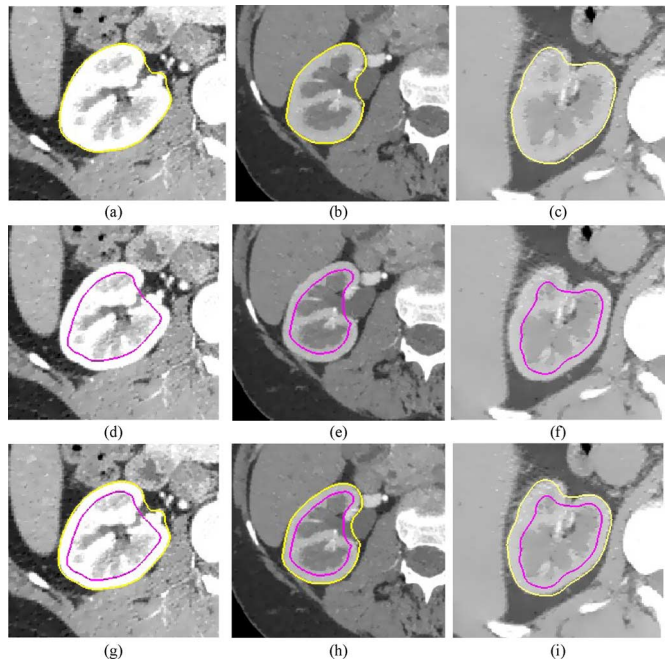

Fig. 11. Contours of surface extraction result. Each column represents one kidney data segmentation result, optimized from the initialized shapes in Fig. 6. The meanings of lines in different colors are the same with Fig. 9.

B. Thresholding and Connected Region Detection

After graying, a simple thresholding technique based on the gray statistical distribution can be applied on the gray renal cortex to remove the nontarget region around the renal pelvis. Then, we use some morphological operations and connected region detection to fill holes and make the renal cortex a simply connected region, which also means refining the renal cortex segmentation results.

After the renal cortex refining procedure, the final renal cortex segmentation results can be generated eventually. Fig. 12 displays some examples of the segmented renal cortex volume, which are refined results of those surfaces in Fig. 11.

VI. Experiments and Discussions

A. Data Sets

For this study, data was taken from a clinical CT dataset containing 17 images. Each case contains 61–396 slices due to the different cross-section spacing (0.5–2.5 mm) and the protocol of different CT scanners. Each slice consists of 512×512 pixels, while the pixel size varied from 0.62 to 0.78 mm. Our method was implemented on a 32-bit desktop PC (2.33 GHz Core 2 and 2 GB RAM) based on the medical imaging toolkit [37] (MITK, http://www.mitk.net/).

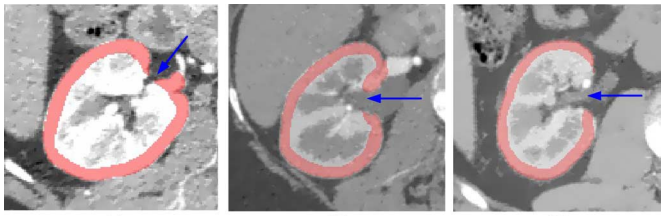

Fig. 12. Renal cortex segmentation results. The red region indicates our segmentation result, and the blue arrows indicate the renal pelvis. The three renal cortex volumes correspond to the refined segmentation of those surfaces in Fig. 11.

TABLE I
PARAMETER SETTINGS

Steps	Parameter Settings
Initialization	$\lambda = 10$, $t = 0.1$, iters 30;
Using	$n = 16$, model radius 0.3, sample number 41, landmarks 2562;
Implicit Shape	$\sigma = 10mm$;
Registration	maxStepSize 1.0mm, minStepSize 0.2mm, maxIters 250
Multiple	Outer surface: $N_0 = 31$, $\Delta_0 = 1$;
Surfaces	Inner surface: $N_1 = 41$, $\Delta_1 = 1$;
Graph	$M = 2562$, $d_j \in [2, 10]mm$, $[T_{min} = 2cm, T_{max} = 20cm]$;
Searching	$\sigma_f = 0.5$, $\alpha = 0.5$, $\gamma = 0.25$

To allow for a quantitative evaluation of the performance of the proposed method, the whole right kidney, the renal cortex and the inside region of renal cortex were manually segmented by a clinician to generate the reference images (ground truth). The manually segmented whole kidneys were also used to construct the average shape, while the manually segmented renal cortexes were used to learn the variation range of renal cortex thickness. The leave-one-out strategy was used in the evaluation.

B. Parameter Settings

In this section we will review detailed parameter settings for each step. In terms of efficiency, Table I lists all of the parameter settings. Particularly, for initialization using implicit shape registration, in shape model training, the model radius, the sample number and the landmarks were specialized for the off-the-shelf software [33], and the training set number n was 16 due to the leave-one-out cross validation strategy; in kidney contour detection, the initial value of t was set empirically at a value where 5% of all voxels are sorted out; the implicit shape registration was accomplished with our 3DMed software [37], the default values were used for all parameters except the maximal and minimum step size and the maximal iterations. For multiple surfaces graph searching, in graph construction, the sampling distance d_j varied from 2 to 10 mm dependent on the sparsity of the local triangular mesh, and for the two sub-graphs (G_0, G_1), the sampling distance d_j was used as the unit of measure for both smoothness constraints (Δ_0, Δ_1), and the learnt renal cortex thickness was defined as $[T_{\min} = 2\ \mathrm{cm}, T_{\max} = 20\ \mathrm{cm}]$ (the range is much bigger than the true value of every data).

Particularly, improper specifications of the geometric constraints may lead to an infeasible problem. Too small constraint values will make the algorithm insensitive to sharp discontinuities, while too large values will result in surface noise and roughness, and loss of the *a priori* shape information [25], [26]. The selection of smoothness constraints (Δ_0, Δ_1) in this work is intuitively based on empirical determination.

C. Evaluations Metrics

We calculate five different quality metrics to evaluate the results of the proposed approach: Dice similarity coefficient (DSC), volumetric overlap error (OE), signed relative volume difference (SVD), average symmetric surface distance (D_{avg}) and average symmetric root mean square (rms) surface distance (D_{rms}). The first metric DSC is a positive performance measure, in which higher value indicates more accurate segmentation, while the other four are negative performance measures, in which lower value reflects more accurate segmentation.

For evaluating the volume overlap, we calculate DSC and OE according to

$$\mathrm{DSC} = \frac{2 \times |V_R \cap V_O|}{|V_R| + |V_O|} \tag{14}$$

$$\mathrm{OE} = 1 - \frac{|V_R \cap V_O|}{|V_R \cup V_O|} \tag{15}$$

where V_R and V_O are the manually segmented reference image and the segmentation result by our approach respectively, while the intersection operation $\cap$ and union operation $\cup$ are the voxel-wise minimum and maximum operation respectively, and $|V|$ is the number of voxels in region V.

To reveal if a result tends to over or under segmented, we calculate SVD according to

$$\mathrm{SVD} = \frac{|V_O| - |V_R|}{|V_R|}. \tag{16}$$

To account for the global and local disagreement between the reference image and the segmentation result image, we calculate D_{avg} and D_{rms} according to

$$D_{\mathrm{avg}} = \frac{\sum_{p_r \in S_R} D(p_r, S_O) + \sum_{p_o \in S_O} D(p_o, S_R)}{|S_R| + |S_O|} \tag{17}$$

$$D_{\mathrm{rms}} = \sqrt{\frac{\sum_{p_r \in S_R} D^2(p_r, S_O) + \sum_{p_o \in S_O} D^2(p_o, S_R)}{|S_R| + |S_O|}} \tag{18}$$

where S_R and S_O represent the surfaces of V_R and V_O, and $D(p, S)$ refers to the minimum Euclidean distance between an arbitrary point p and shape S as in (3).

D. Performance Evaluations

To evaluate the performance of automatic renal cortex segmentation, three different experiments were performed.

1) Evaluation of Initialization Using Implicit Shape Registration: The renal cortex segmentation method presented in this paper is highly relied on the initialization. If initialization fails, the method will mostly perform poorly. An implicit shape registration method is applied to initialize the kidney shape in the test scans, instead of the manual localization in our previous work [10], and results from the two methods are demonstrated in Fig. 13. To analyze the results quantitatively, we convert both initialized shapes into volumes with the same dimensions and spacing as the original CT datasets, and compute the DSC using the manually segmented kidney as reference. The DSC value for

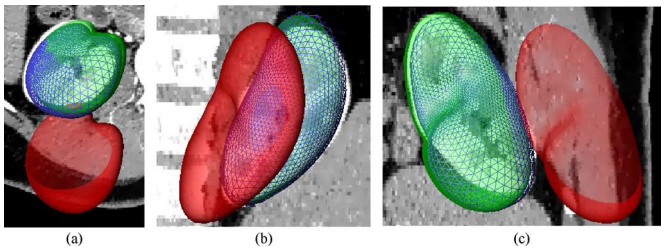

Fig. 13. Initialization result from the implicit shape registration method and manual localization. The red semitransparent surface denotes the average shape (the "Average Shape" in Fig. 2), and the green one denotes the initialized shape using the implicit shape registration method (the "Initialized Shape" in Fig. 2), while the blue wire frame denotes the manual localization result. (a) Transverse view. (b) Coronal view. (c) Sagittal view.

TABLE II
METRICS RESULTS (Mean ± SD)

Metrics	*DSC*(%)	*OE*(%)	*SVD*(%)	D_{avg}(mm)	D_{RMS}(mm)
Outer Surface	96.55±1.77	2.43±2.22	1.42±2.44	0.14±0.09	0.66±0.61
Inner Surface	92.27±2.24	6.55±5.03	-5.91±5.44	0.43±0.30	1.11±0.73
Renal Cortex Mask	87.62±1.79	4.83±4.64	3.09±2.38	0.21±0.13	0.81±0.71
Final Renal Cortex	90.50±1.19	4.38±3.93	2.37±1.72	0.18±0.11	0.80±0.64

the manual localization is $80.77\% \pm 5.20\%$ (MEAN ± SD), while the value for the implicit shape registration method is $80.66\% \pm 6.76\%$ (MEAN ± SD). Although the result of the automated method is slightly worse than that of manual localization, it is sufficient for the following surface graph searching phase.

2) Evaluation of Multiple Surfaces Graph Searching: Since it is the key part of the whole segmentation method, we conducted a more comprehensive evaluation. Manual segmentations of the whole kidney, the renal cortex and the inside region of renal cortex were used as references, and compared with the extracted outer surface volume, the extracted inner surface volume and the binary renal cortex mask (Section V), using five metrics: DSC, OE, SVD, D_{avg}, and D_{rms}. Note that although the binary renal cortex mask is generated in Section V, it mostly depends on the surfaces extraction result in Section IV because Section V only refines the segmentation to a limited extent. These metrics are summarized in Table II. The DSC values for the initialized shape ($80.66\% \pm 6.76\%$) and the extracted outer surface ($96.55\% \pm 1.77\%$), which demonstrates the effectiveness of multiple surfaces graph searching on detecting the borders of the renal cortex, especially for the outer border.

Comparing the second, third and fourth row in Table II, we find that the performance of outer surface segmentation is the best, then the overall performance, and last is that of inner surface segmentation. Such result implies that the inner surface segmentation drag the overall performance to a certain extent, and some inner surface segmentation bias can be intuitively discovered from Fig. 14 (see red arrows). As stated in Section I-A, the renal cortex and renal column are almost fused as one connected component, which determines that the continuous inner border of renal cortex rarely exists. This property, together with its own low intensity contrast, makes the inner surface segmentation more challenging than the segmentation of the outer surface.

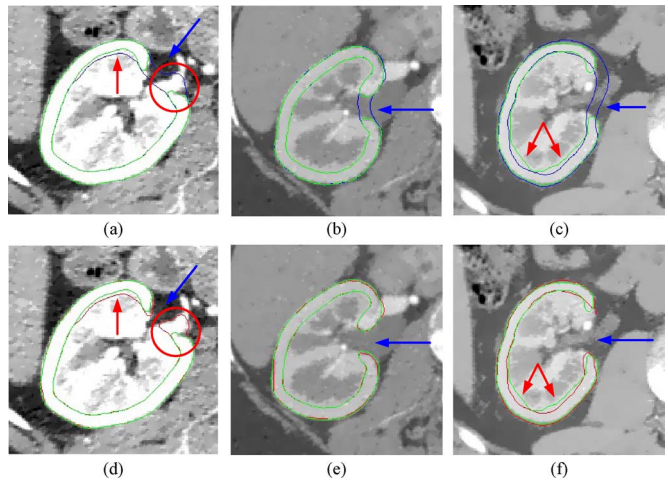

Fig. 14. Renal cortex segmentation results before and after renal cortex refining. Each column represents a single kidney data segmentation result corresponding to the three initialized shapes in Fig. 6, the experimental results of different filters in Fig. 10 and the three columns of the extracted surfaces in Fig. 11. As in Fig. 10, from left to right, it presents a poor quality case (left), a good quality case (middle), and a medium quality case (right). The top row represents the renal cortex segmentation result before renal cortex refining, namely the binary renal cortex mask, and the bottom row represents the result after refining, namely the final renal cortex volume. The green lines denote manual segmentation of the renal cortex, and the blue lines in the top row denote the binary renal cortex mask, while the red lines in the bottom row denote the final renal cortex volume. The blue arrows indicate the renal pelvis, while the red arrows indicate the inner surface segmentation bias. The red circles indicate the false positive responses of renal cortex segmentation.

3) Evaluation of Renal Cortex Refining: Since its purpose is to improve the renal cortex segmentation, we can compare the final renal cortex volume with the previous binary renal cortex mask to evaluate its performance. The results are presented in Fig. 14 and summarized in the last row of Table II. Comparing the last two rows in Table II, we find that the renal cortex refining substantially improves the segmentation accuracy. Furthermore, we find some false positive responses (red circles in Fig. 14) which might be present in the final renal cortex volume. The intensity distributions of the renal pelvis may be close to that of the renal cortex in some CT images. If the two structures are also adjacent in space, it becomes more difficult to distinguish them.

Comparing the three rows in Figs. 10 and 14, we find that the image quality and spatial relationship among different kidney structures such as the space adjacency of renal pelvis and renal cortex in Fig. 14(a) and (d), affect the renal cortex segmentation result. An experiment was performed to analyze the stability and robustness of the proposed approach. We compare the extracted outer and inner surface volumes, the binary renal cortex mask and the final renal cortex volume of the three sample data sets with their corresponding manual segmentation results using the five metrics as above. The results are presented in Fig. 14 and summarized in Table III, in which "Poor Case," "Good Case," and "Medium Case" represent the three kidney images in Fig. 14, respectively.

E. Computation Time

The whole method presented in this paper takes on average 25 min per dataset. Table IV shows the average computational

TABLE III
SAMPLE RESULTS (POOR CASE/GOOD CASE/MEDIUM CASE)

Metrics	*DSC*(%)	*OE*(%)	*SVD*(%)	D_{avg}(mm)	D_{RMS}(mm)
Outer Surface	94.62/98.34/96.55	4.64/0.20/2.13	4.00/-0.82/1.55	0.19/0.09/0.15	1.39/0.30/0.81
Inner Surface	90.81/94.71/92.33	11.36/1.31/6.53	-10.74/-1.39/-5.18	0.82/0.23/0.43	1.64/0.69/1.30
Renal Cortex Mask	85.18/89.88/87.59	9.16/0.73/4.64	5.44/1.19/3.23	0.40/0.18/0.22	1.33/0.24/0.70
Final Renal Cortex	89.25/92.44/91.42	8.95/0.62/3.51	4.62/0.90/2.42	0.34/0.13/0.21	1.09/0.11/0.64

TABLE IV
COMPUTATION TIME

Steps	Time
Nonlinear Diffusion Filtering	20mins
Initialization Using Implicit Shape Registration	10secs
Multiple Surfaces Graph Searching	5mins
Renal Cortex Refining	6secs
Total	∼25mins

time needed for each step of the algorithm. The training time for shape model training is not included, and our implementations were not optimized for speed, and the values we give here are simply indications of the running time. It can be seen that the nonlinear diffusion filtering is the most computationally expensive part of the algorithm, taking 80% of the whole computation time. Although nonlinear diffusion filtering smoothes the image and reduces noise, which is important to the following operations and determines the final results to a certain extent, we will still be able to find some other image enhancing technique which could shorten the processing time while preserving the effect. The computation time of other steps in our method is very competitive. Take the initialization using implicit shape registration for example, as reviewed in [19], other approaches such as the GHT [20], [21], EA [22], [23] and particle filtering [24] usually take several minutes or even half an hour to locate the shape model.

VII. CONCLUSION AND FUTURE WORK

In this paper, we have proposed a novel approach for automatic renal cortex segmentation which effectively integrates the implicit shape registration based initialization and the extended multiple surfaces graph search method with incorporation of physical constraints. This approach could tackle the problems brought by the special characteristics of the kidney's anatomical structure as discussed in Section I-A. We evaluated the method on 17 clinical CT scans with the leave-one-out strategy. The experimental results showed that our method is effective and accurate in the presence of weak boundaries and structural ambiguities.

We propose an implicit shape registration method for the kidney shape initialization. This new technique makes the whole renal cortex segmentation approach fully automatic compared against the manual localization used in our previous work [10]. The initialization results in Figs. 6 and 13 reveal the good performance compared against manual localization. Meanwhile, the computation time of this method is very competitive, which determines that it could be easily extended to other applications.

In order to better restrain the intensity proximity of the renal cortex and renal column (detailed in Section I-A), we extend the multiple surfaces graph search approach to allow for varying sampling distances and physical separation constraints, instead of the traditional fixed sampling distance and numerical separation constraints as in [10], [25]–[27]. The renal cortex outer and inner surfaces extraction results in Fig. 11 and Table II demonstrate the effectiveness of our extended multiple surfaces graph search method. The incorporation of physical constraints can also be introduced to other applications if the corresponding *a priori* information is available.

In order to detect and reduce incorrect segmentation pixels introduced by the nonfully closed structure around renal pelvis, we design a renal cortex refining procedure which consists of a series of image processing operations. The final renal cortex segmentation results in Figs. 12 and 14 and Table II reveal the substantial accuracy improvement brought about by the renal cortex refining.

In summary, our major contributions are three-fold.

1) We present an implicit shape registration based shape model initialization method which makes the renal cortex segmentation fully automatic substantially.
2) We propose a novel extension to the multiple surfaces graph search approach to allow for varying sampling distances and physical separation constraints, which can better restrain the intensity proximity of the renal cortex and renal column.
3) We design a renal cortex refining procedure which could detect and reduce incorrect segmentation pixels around the renal pelvis.

Although encouraging results have been achieved, there still exists some systematic bias (see red arrows in Fig. 14) or even segmentation error (see red circles in Fig. 14). It is important to realize the difficulty of the renal cortex segmentation task taking into account the special characteristics of the kidney's anatomical structure. Therefore in our future work, we will focus on: 1) study the attributes of the renal cortex and propose better graph construction and cost functions to ease the segmentation bias, especially the adaptive selection of smoothness constraints (Δ_0, Δ_1); 2) design a more accurate and effective renal cortex refining procedure to detect and reduce incorrect segmentation pixels around the renal pelvis; 3) find or design other image enhancing technique which could shorten the processing time while preserving the result; and 4) use more objective validation with both left and right kidney datasets and reference standard acquired from multiple experts.

REFERENCES

[1] M. D. Beland, N. L. Walle, J. T. Machan, and J. J. Cronan, "Renal cortical thickness measured at ultrasound: Is it better than renal length as an indicator of renal function in chronic kidney disease?," *Am. J. Roentgenol.*, vol. 195, no. 2, pp. 146–149, 2010.

[2] N. S. Muto, T. Kamishima, A. A. Harris, F. Kato, Y. Onodera, S. Terae, and H. Shirato, "Renal cortical volume measured using automatic contouring software for computed tomography and its relationship with BMI, age and renal function," *Eur. J. Radiol.*, vol. 78, no. 1, pp. 151–156, 2011.

[3] F. Artunc, S. Yildiz, C. Rossi, A. Boss, H. Dittmann, H. P. Schlemmer, T. Risler, and N. Heyne, "Simultaneous evaluation of renal morphology and function in live kidney donors using dynamic magnetic resonance imaging," *Nephrol. Dial. Transplant.*, vol. 25, no. 6, pp. 1986–1991, 2010.

[4] L. A. Stevens, J. Coresh, T. Greene, and A. S. Levey, "Assessing kidney function—Measured and estimated glomerular filtration rate," *N. Engl. J. Med.*, vol. 354, no. 23, pp. 2473–2483, 2006.

[5] J. Xie, Y. F. Jiang, and H. T. Tsui, "Segmentation of kidney from ultrasound images based on texture and shape priors," *IEEE Trans. Med. Imag.*, vol. 24, no. 1, pp. 45–57, Jan. 2005.

[6] D. Lin, C. Lei, and S. Hung, "Computer-aided kidney segmentation on abdominal CT images," *IEEE Trans. Inf. Technol. Biomed.*, vol. 10, no. 1, pp. 59–65, Jan. 2006.

[7] M. Spiegel, D. Hahn, V. Daum, J. Wasza, and J. Hornegger, "Segmentation of kidneys using a new active shape model generation technique based on non-rigid image registration," *Comput. Med. Imag. Graph.*, vol. 33, no. 1, pp. 29–39, 2009.

[8] M. Freiman, A. Kronman, S. J. Esses, L. Joskowicz, and J. Sosna, "Non-parametric iterative model constraint graph min-cut for automatic kidney segmentation," in *Proc. 13th Int. Conf. Med. Image Computing Computer Assist. Intervent. (MICCAI)*, 2010, pp. 73–80.

[9] O. Gloger, K. D. Tonnies, V. Liebscher, B. Kugelmann, R. Laqua, and H. Volzke, "Prior shape level set segmentation on multistep generated probability maps of MR datasets for fully automatic kidney parenchyma volumetry," *IEEE Trans. Med. Imag.*, vol. 31, no. 2, pp. 312–325, Feb. 2012.

[10] X. Li, X. Chen, J. Yao, X. Zhang, and J. Tian, "Renal cortex segmentation using optimal surface search with novel graph construction," in *Proc. 14th Int. Conf. Med. Image Computing Computer Assist. Intervent. (MICCAI)*, 2011, pp. 387–394.

[11] B. Tsagaan, A. Shimizu, H. Kobatake, and K. Miyakawa, "An automated segmentation method of kidney using statistical information," in *Proc. 5th Int. Conf. Med. Image Computing Computer Assist. Intervent. (MICCAI)*, 2002, pp. 556–563.

[12] W. Touhami, D. Boukerroui, and J. Cocquerez, "Fully automatic kidneys detection in 2D CT images: A statistical approach," in *Proc. 8th Int. Conf. Med. Image Computing Computer Assist. Intervent. (MICCAI)*, 2005, pp. 262–269.

[13] H. K. Koh, S. Weijia, B. Shuter, and A. A. Kassim, "Segmentation of kidney cortex in MRI studies using a constrained morphological 3-D h-maxima transform," in *Proc. 9th Int. Conf. Control, Automat., Robot. Vis. (ICARCV)*, 2006, pp. 1–5.

[14] S. Yuksel, A. El-Baz, and A. Farag, "A kidney segmentation framework for dynamic contrast enhanced magnetic resonance imaging," *J. Vib. Control*, vol. 13, no. 9–10, pp. 1505–1516, 2007.

[15] W. Cai, N. Holalkere, G. Harris, D. Sahani, and H. Yoshida, "Dynamic-threshold level set method for volumetry of porcine kidney in CT images: In vivo and ex vivo assessment of the accuracy of volume measurement," *Acad. Radiol.*, vol. 14, no. 7, pp. 890–896, 2007.

[16] H. Abdelmunim, A. Farag, W. Miller, and M. AboelGhar, "A kidney segmentation approach from DCR-MRI using level sets," in *Proc. 21th IEEE Comput. Soc. Conf. Comput. Vis. Pattern Recognit. (CVPR)*, 2008, pp. 566–571.

[17] F. G. Zoellner, R. Sancee, P. Rogelj, M. J. Ledesma-Carbayo, J. Rovik, A. Santos, and A. Lundervold, "Assessment of 3-D DCE-MRI of the kidneys using non-rigid image registration and segmentation of voxel time courses," *Comput. Med. Imag. Graph.*, vol. 33, no. 3, pp. 171–181, 2009.

[18] D. Stalling, M. Westerhoff, and H. Hege, *Amira: A Highly Interactive System for Visual Data Analysis*. New York: Elsevier, 2005.

[19] T. Heimann and H. Meinzer, "Statistical shape models for 3-D medical image segmentation: A review," *Med. Image Anal.*, vol. 13, no. 4, pp. 543–563, 2009.

[20] X. Zhang, J. Tian, K. Deng, Y. Wu, and X. Li, "Automatic liver segmentation using a statistical shape model with optimal surface detection," *IEEE Trans. Biomed. Eng.*, vol. 57, no. 10, pp. 2622–2626, Oct. 2010.

[21] O. Ecabert, J. Peters, H. Schramm, C. Lorenz, J. von Berg, M. J. Walker, M. Vembar, M. E. Olszewski, K. Subramanyan, G. Lavi, and J. Weese, "Automatic model-based segmentation of the heart in CT images," *IEEE Trans. Med. Imag.*, vol. 57, no. 10, pp. 2622–2626, Oct. 2010.

[22] A. Pitiot, A. W. Toga, and P. M. Thompson, "Adaptive elastic segmentation of brain MRI via shape-model-guided evolutionary programming," *IEEE Trans. Med. Imag.*, vol. 21, no. 8, pp. 910–923, Aug. 2002.

[23] T. Heimann, S. Munzing, H. Meinzer, and I. Wolf, "A shape-guided deformable model with evolutionary algorithm initialization for 3-D soft tissue segmentation," in *Proc. 20th Inf. Process. Med. Imag. (IPMI)*, 2007, pp. 1–12.

[24] M. D. Bruijne and M. Nielsen, "Multi-object segmentation using shape particles," in *Proc. 19th Inf. Process. Med. Imag. (IPMI)*, 2005, pp. 59–127.

[25] K. Li, X. D. Wu, D. Z. Chen, and M. Sonka, "Optimal surface segmentation in volumetric images—A graph-theoretic approach," *IEEE Trans. Pattern Anal. Mach. Intell.*, vol. 28, no. 1, pp. 119–134, Jan. 2006.

[26] Y. Yin, X. M. Zhang, R. Williams, X. D. Wu, D. D. Anderson, and M. Sonka, "Logismos-layered optimal graph image segmentation of multiple objects and surfaces: Cartilage segmentation in the knee joint," *IEEE Trans. Med. Imag.*, vol. 29, no. 12, pp. 2023–2037, Dec. 2010.

[27] M. Garvin, M. Abramoff, X. D. Wu, S. R. Russell, T. L. Burns, and M. Sonka, "Automated 3-D intraretinal layer segmentation of macular spectral-domain optical coherence tomography images," *IEEE Trans. Med. Imag.*, vol. 28, no. 9, pp. 1436–1447, Sep. 2009.

[28] Y. Boykov and V. Kolmogorov, "An experimental comparison of min-cut/max-flow algorithms for energy minimization in vision," *IEEE Trans. Pattern Anal. Mach. Intell.*, vol. 26, no. 9, pp. 1124–1137, Sep. 2004.

[29] X. Huang, N. Paragios, and D. N. Metaxas, "Shape registration in implicit spaces using information theory and free form deformations," *IEEE Trans. Pattern Anal. Mach. Intell.*, vol. 28, no. 8, pp. 1303–1318, Aug. 2006.

[30] X. Li, X. Chen, J. Yao, X. Zhang, and J. Tian, "Incorporation of physical constraint in optimal surface search for renal cortex segmentation," in *Proc. SPIE Med. Imag.*, 2012.

[31] J. Weickert, B. Romeny, and M. Viergever, "Efficient and reliable schemes for nonlinear diffusion filtering," *IEEE Trans. Image Process.*, vol. 7, no. 3, pp. 398–410, Mar. 1998.

[32] W. E. Lorensen and H. E. Cline, "Marching cubes: A high resolution 3-D surface construction algorithm," in *Proc. ACM SIGGRAPH Comput. Graph.*, 1987, pp. 163–169.

[33] T. Heimann, I. Oguz, I. Wolf, M. Styner, and H.-P. Meinzer, "Implementing the automatic generation of 3-D statistical shape models with ITK," in *Proc. MICCAI Open Science Workshop*, 2006, pp. 1–22.

[34] A. V. Nasonov and A. S. Krylov, "Fast super-resolution using weighted median filtering," in *Proc. 20th Int. Conf. Pattern Recognit. (ICPR)*, 2010, pp. 2230–2233.

[35] S. Osher and J. A. Sethian, "Fronts propagating with curvature-dependent speed: Algorithms based on Hamilton-Jacobi formulations," *J. Comput. Phys.*, vol. 79, no. 1, pp. 12–49, 1988.

[36] N. Paragios, M. Rousson, and V. Ramesh, "Matching distance functions: A shape-to-area variational approach for global-to-local registration," in *Proc. 7th Eur. Conf. Comput. Vis. (ECCV)*, 2002, pp. 813–815.

[37] J. Tian, J. Xue, Y. Dai, J. Chen, and J. Zheng, "A novel software platform for medical image processing and analyzing," *IEEE Trans. Inf. Technol. Biomed.*, vol. 12, no. 6, pp. 800–812, Nov. 2008.

[38] D. Scharstein, "Matching images by comparing their gradient fields," in *Proc. 12th Int. Conf. Pattern Recognit. (ICPR)*, 1994, pp. 572–575.

[39] Y. Sato, C. Westin, A. Bhalerao, S. Nakajima, N. Shiraga, S. Tamura, and R. Kikinis, "Tissue classification based on 3-D local intensity structures for volume rendering," *IEEE Trans. Vis. Comput. Graph.*, vol. 6, no. 2, pp. 160–180, 2002.

[40] Y. Sato, S. Nakajima, N. Shiraga, H. Atsumi, S. Yoshida, T. Koller, G. Gerig, and R. Kikinis, "Three-dimensional multi-scale line filter for segmentation and visualization of curvilinear structures in medical images," *Med. Image Anal.*, vol. 2, no. 2, pp. 143–168, 1998.